

A Soft-Bodied Aerial Robot for Collision Resilience and Contact-Reactive Perching

Pham H. Nguyen⁺, Karishma Patnaik⁺,
Shatadal Mishra, Panagiotis Polygerinos and Wenlong Zhang^{*}

Abstract—Compared to their biological counterparts, aerial robots demonstrate limited capabilities when tasked to interact in unstructured environments. Very often, the limitation lies in their inability to tolerate collisions and to successfully land, or perch, on objects of unknown shape. Over the past years, efforts to address this have introduced designs that incorporate mechanical impact protection and grasping/perching structures at the cost of reduced agility and flight time due to added weight and bulkiness. In this work, we develop a fabric-based, soft-bodied aerial robot (SoBAR) composed of both contact-reactive perching and embodied impact protection structures while remaining lightweight and streamlined. The robot is capable to 1) pneumatically vary its body stiffness for collision resilience and 2) utilize a hybrid fabric-based, bistable (HFB) grasper to perform passive grasping. When compared to conventional rigid drone frames the SoBAR successfully demonstrates its ability to dissipate impact from head-on collisions and maintain flight stability without any structural damage. Furthermore, in dynamic perching scenarios the HFB grasper is capable to convert impact energy upon contact into firm grasp through rapid body shape conforming in less than 4ms. We exhaustively study and offer insights for this novel perching scheme through grasping characterization, grasp wrench analysis, and experimental grasping validations in objects with various shapes. Finally, we demonstrate the complete control pipeline for SoBAR to approach an object, dynamically perch on it, recover from it, and land.

Index Terms—Soft Aerial Robots, Reconfigurable Robots, Passive Dynamics, Soft Robotics, Grasping, Adaptive Perching.

I. INTRODUCTION

Perching highlights the ability for aerial robots to save energy and maintain a vantage position for monitoring or surveillance [1]. Existing aerial robots coordinate perching mechanisms and flight dynamics to achieve perching [2]. Various bio-inspired perching mechanisms have been developed for aerial robots, including electrostatic adhesion [3], dry adhesion [4], [5], microspines and strings [6]–[8], activated preloaded spike vertical surfaces [9], and claw-like avian-inspired graspers [10]–[16]. Nature, however, calls attention

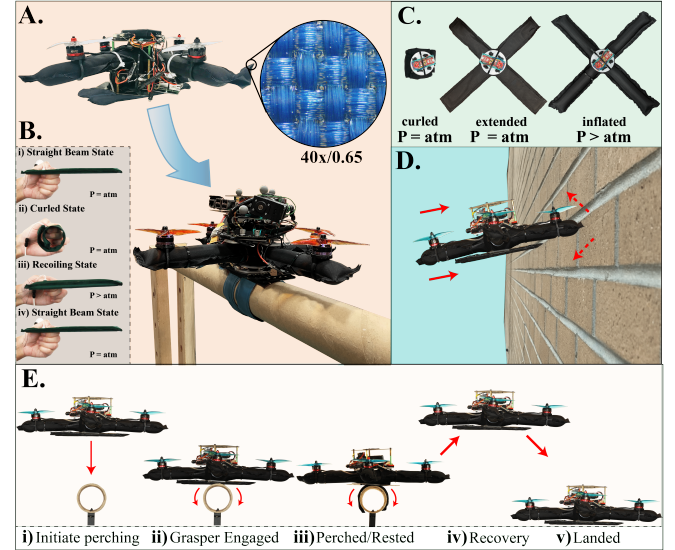


Fig. 1. (A) Flying and dynamic collision-based perching sequence. The woven fabric utilized is highlighted under a microscope. (B) Perching mechanism sequence from straight beam to curled to recovery state. (C) Soft frame from a deflated stored state to an inflated and rigid state. (D) Head-on wall collision with SoBAR. (E) Dynamic perching to recovery to landing sequence of SoBAR.

to various physically intelligent features that can enhance the proficiency of dynamic aerial robot perching and grasping [17]. Birds and bats enter a coordinated post-stall maneuver, to maintain a constant rate of approach in combination with a high angle of attack [18]–[20]. At impact, their feet clasp the irregular perch and their legs bend to absorb their momentum [12], [21], [22]. Their feet also utilize a passive tendon locking mechanism, so no additional energy is wasted during perching [23]. Even smaller insects, like flies, utilize a combination of collision and perching, and their compliant bodies help dampen the perching impact [24].

However, there is often a dissociation between controlled collision and dynamic perching in the existing design of aerial robots, as the rigid-body structures are not good at mitigating collision impact incurred during dynamic perching. Furthermore, avian-inspired graspers are limited to perching on cylindrical-shaped structures [13], [25]. Recent work has started taking into account controlled collision during dynamic perching. Roderick et. al [15], highlights a robot that combines an adaptive avian-inspired grasper with embedded features (claws), and legs that absorb the robot's momentum resulted from perching impact. Kirchgeorg et. al [16] explores the

K. Patnaik and W. Zhang are with the Polytechnic School, Ira A. Fulton Schools of Engineering, Arizona State University, Mesa, AZ 85212, USA. {kpatnaik, wenlong.zhang}@asu.edu

P. H. Nguyen was with the Polytechnic School, Arizona State University. He is currently with the Aerial Robotics Lab, Imperial College London, UK. n.pham@imperial.ac.uk

S. Mishra was with the Polytechnic School, Arizona State University. He is currently with Toyota InfoTech R&D Labs, Mountain View, CA, USA. smishr13@asu.edu

P. Polygerinos is currently with Control Systems and Robotics Laboratory (CSRL), Hellenic Mediterranean University, Crete, Greece. polygerinos@hmu.gr

⁺ The first two authors contribute equally to this work.

^{*} Address all correspondence to this author.

use of an external protective exoskeleton, along with a high-friction, passive, hook-and-hang perching mechanism. These robots, however, do not extensively quantify their ability to mitigate the high impact in collision-based perching. They also limit their grasping targets to branches with circular cross-sections.

Along with dynamic perching, aerial robots also have to deal with unexpected interactions in obstacle-laden environments with poor visual conditions. Therefore, collisions are inevitable even with state-of-the-art collision avoidance and computer vision systems [26], [27]. With aerial robots, high-energy impacts or collisions can lead to structural damage or loss of control, resulting in crashes. Therefore, researchers have developed collision-resilient aerial robots with compliant bodies to sustain collisions whilst remaining stable in the air and/or surviving structural damage after crashing [28]–[31].

To approach the problem of collision resilience and safe perching, soft robotics has emerged as a promising solution [32]–[34]. Compliant materials have been utilized to design soft or foldable wings [35]–[39], deformable rotors [40], compliant joints and armatures [28], [41]–[45], and compliant graspers or landing gears [8], [46]–[53]. These soft solutions for perching and grasping, however, are often limited by their load bearing capabilities and slow grasping speeds. The former limits their ability to maintain a strong grasp on objects or carry meaningful payloads. Due to their limited grasping speeds, they resort to hovering closely or landing on the perch prior to grasping. They also sometimes require active actuation to maintain constant grasping or perching position, which reduces the overall system efficiency.

In this work, we developed a soft-bodied aerial robot (SoBAR) capable of effectively mitigating high-impact and head-on collisions with the environment, as well as absorbing impact forces during collision-based perching, as seen in Figs. 1A and D. SoBAR’s lightweight soft-bodied frame is capable of modulating its stiffness pneumatically, for contact resilience and flight stability, as seen in Fig. 1C. Due to the utilization of high-strength woven fabric, the robot is robust to environmental interactions but still easily stowable, shown in Fig. 1D. The process of setting up and reassembling SoBAR takes approximately 4 minutes, making it effortlessly portable, as highlighted in Appendix A and Supplementary Video 1.

In parallel to the collision-mitigation abilities we introduce a hybrid fabric-based bistable (HFB) grasper design, which reacts to impact upon contact with the perching surface, as illustrated in Fig. 1B. Utilizing a snap-through buckling instability in its passive design, the grasper absorbs the impact energy and uses it to transform into a continuum closed-form grasping shape in about 4ms. Further, the passive grasper does not utilize any additional energy to maintain grasping, and can be pneumatically retracted in less than 3s. Finally, we successfully demonstrate the ability of SoBAR to autonomously perch and recover, on various sized and shaped objects, as seen in Fig. 1E. In summary, this work contributes to:

- 1) A new class of soft-bodied aerial robots (SoBAR) capable of effectively absorbing impact forces from collisions and contact-based perching.
- 2) An adaptable, passive, hybrid fabric-based bistable (HFB) grasper capable of rapid dynamic perching on various shaped and sized perches.
- 3) A planning and control strategy for SoBAR to approach, perch, recover and land utilizing the HFB grasper.

II. MATERIALS AND METHODS

A. Design of Soft-Bodied Structure

To develop SoBAR’s pneumatic frame we opted for a standard “×” or “+” configuration to benchmark the system’s mechanical resilience in one arm or two arm collisions. We designed SoBAR’s frame to be geometrically similar to DJI F450’s standard rigid frame (319mm×319mm), for comparison in collision tests. SoBAR’s and DJI’s frames weigh 10g and 120g, respectively.

To develop the soft-bodied frame, we took inspiration from the thin-walled, hollow pneumatic bones that are found in bird wings [54]. These pneumatic bones are connected to their pulmonary system that regulates air to increase skeletal buoyancy, making it extremely lightweight but still very resistant against external loads [55]. Combining this idea with our previous work on soft fabric-based actuators [56]–[58], we opted to evoke a soft-bodied structure based on thin-walled, soft inflatable fabric beams. Such pneumatically driven structures are shown to be mechanically resilient to external interactions and can absorb impact-induced energies. These characteristics enable SoBAR to handle high-speed collisions, collision-based perching, and emergency landings. Additionally, by having a collision-safe air frame, eliminates the need for a cage-like structure around the aerial robot in applications where no humans are present, thus making the design compact and efficient. The intrinsically soft platform we designed can also vary in stiffness through pneumatic activation. Fig. 1D shows that at zero internal pressure, the frame is completely collapsible and each arm can compress from 20.5cm to 3cm; a reduction in length of 85% (also shown in Supplementary Video 1). For flight, the frame is inflated to its maximum stiffness to reduce undesired oscillations, instabilities, or slow flight maneuver responses. The SoBAR frame can absorb impact through deformation, which extends the impact time with the perching objects to support the collision-based passive perching maneuver with the HFB grasper, as seen in Fig. 1A. Fabrication of the SoBAR’s frame is detailed in Fig. 2A and Appendix B.

B. Design of the HFB Grasper

The HFB perching structure is designed with a TPU-coated nylon fabric external structure encasing pre-formed bistable metal steels, capable of converting high-impact energy and instantly reacting to the contact, in order to go from a straight beam to a rapidly curling state, as seen in Fig. 1B. Each perching structure is made of multiple HFB actuators placed in possible perching orientations, as in in Fig. 2B and Fig. 2A(iv).

The design combines the energy storage nature of deformable spring steels and fabric-based actuators. The bistable spring steel, when activated, leads to power amplification and rapid curling movements that are highly desired for grasping.

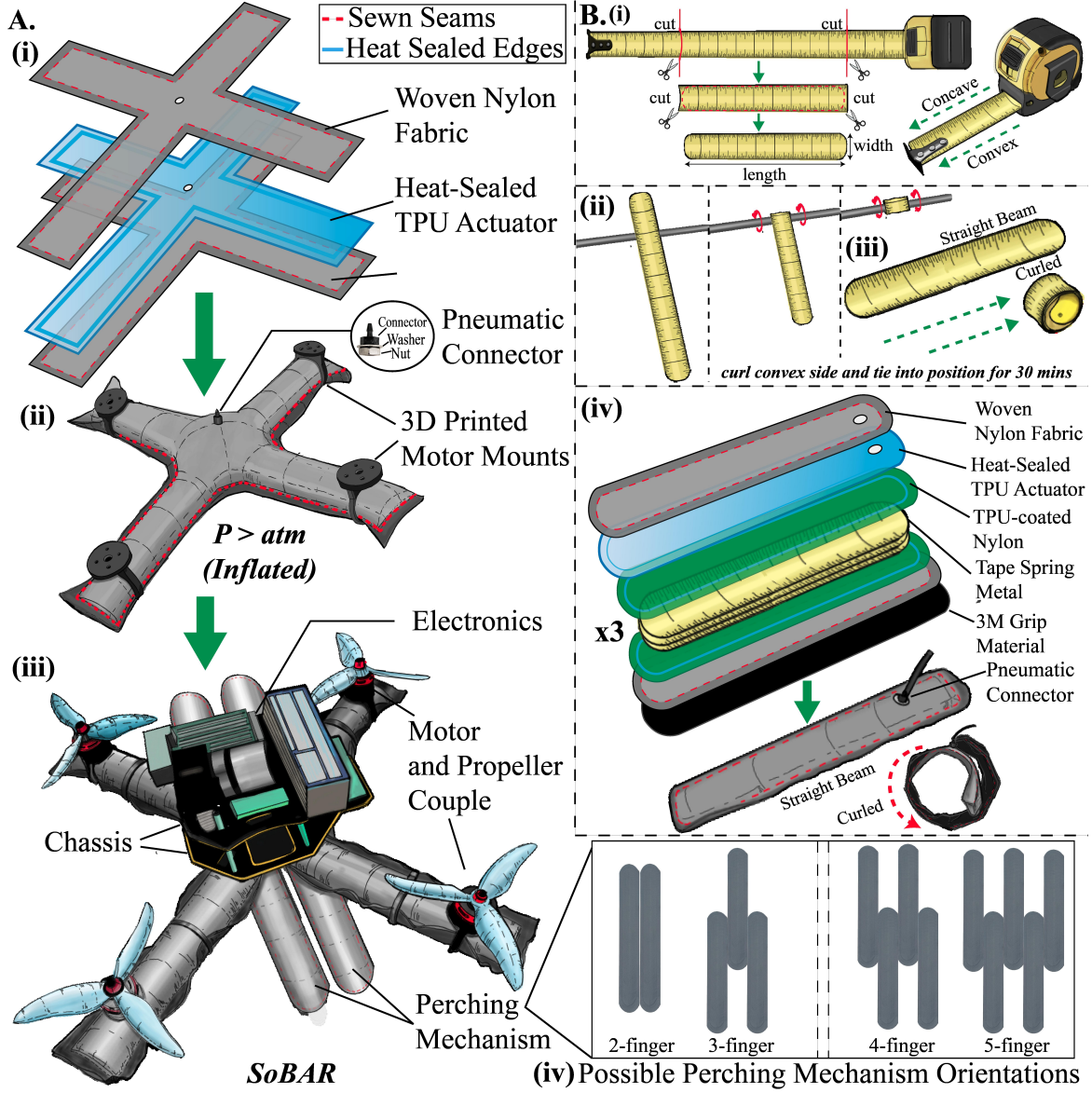


Fig. 2. (A) Fabrication steps for SoBAR. (i) First, align the woven fabric and heat-sealed actuator, after laser cutting. The woven fabric sheets are then sewn along the edges, utilizing a super-imposed seam, and the heat-sealed actuator is inserted, to create the soft frame. (ii) Next, the pneumatic connector and 3D-printed motor mounts are added and aligned on the inflated soft-bodied frame. (iii) Finally, mount the propellers and motor pairs, electronics, and the perching mechanism. (iv) Possible perching mechanism orientations made of multiple HFB actuators (B) HFB actuator fabrication. (i) First, prepare the curling bistable mechanism by cutting and forming the spring steel metal. (ii) Next, curl the bistable tape spring, along its convex side, and maintain the position for 30min. (iii) The curling bistable tape spring. (iv) Finally, align the woven fabric, heat-sealed TPU actuator, TPU-coated nylon, three tape springs, and 3M grip material to create a single HFB actuator.

Furthermore, after perching, no further mechanical activation is required. In order to release it from its perched state, the inflatable fabric-based actuator layer allows the system to quickly recoil, to its initial straight beam state, as in Fig. 1B(iv) and Supplementary Video 2. In this state, the grasper can also be utilized as landing skids. Along with its soft-bodied frame, the robot is capable of safe emergency landing situations, as seen in Fig. 1E(v). Fabrication of the HFB grasper is detailed in Appendix B.

C. Hardware Overview

SoBAR's chassis hosts the flight controller, power module, and high-level companion computer, as seen in Fig. 3. The

flight controller monitors and controls the internal pressure of SoBAR's body and the HFB grasper, by utilizing analog pressure sensors and an on-board micro diaphragm pump. The specific hardware and electronics details are further documented in Appendix C. Prior to flight, motor propeller pairs are aligned and the flight controller sensors with the air frame are calibrated through QGroundControl. The experimental setups utilized in this work, including the universal tensile testing machine, the high-speed camera, high-G accelerometer, and motion capture system are detailed in Appendix D.

D. Modeling and Control of SoBAR

As shown in Fig. 5, the rotor thrust is significant enough to introduce slight beam bending of the soft arms that affects

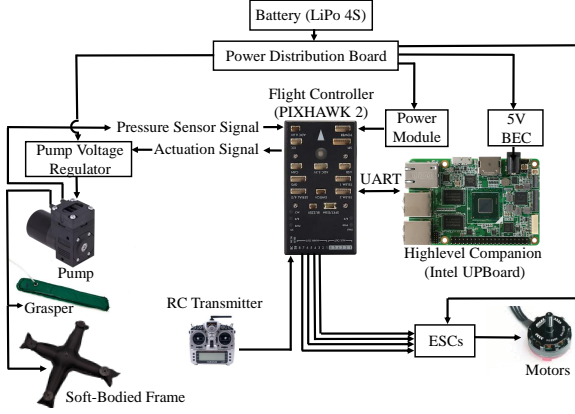


Fig. 3. Electronics diagram of SoBAR. On the right part of the diagram all the necessary components to achieve flight are illustrated. On the left part of the diagram the proposed electro-pneumatic components for the soft frame and perching grasper are shown.

net thrust and SoBAR's flight performance. To address this issue, we model the thrust coefficient as a function of the arm deflection angle and employ the Euler-Bernoulli beam theory [59] to calculate this angle. We then utilize this thrust coefficient in the controller to improve the flight performance.

For inflatable beams without wrinkles [59], the deflection angle, θ_i , is calculated as

$$\begin{aligned} y_{beam} &= \frac{F_i l^3}{3EI}, \\ \theta_i &= -\frac{F_i l^2}{2EI}, \end{aligned} \quad (1)$$

where l , F_i , and I are the arm length, applied thrust, and area moment of inertia of the beam, respectively. y_{beam} is the experimentally measured tip deflection, shown in Fig. 5.

The deflection angle, θ , is then used to estimate the net thrust by

$$f_i = F_i \cos \theta_i, \quad (2)$$

where the thrust loss coefficient is approximated by $\cos \theta_i$. To compute the individual motor commands, we define the following motor speed control allocation mapping matrix, A , to describe the relationship between the net force and torques to individual motor thrusts as below

$$\begin{pmatrix} {}_b f \\ {}_b \mathbf{M} \end{pmatrix} = \underbrace{\begin{pmatrix} 1 & 1 & 1 & 1 \\ 0 & -d & 0 & d \\ d & 0 & -d & 0 \\ -c_{\tau f} & c_{\tau f} & -c_{\tau f} & c_{\tau f} \end{pmatrix}}_A \underbrace{\begin{pmatrix} f_1 \\ f_2 \\ f_3 \\ f_4 \end{pmatrix}}_N, \quad (3)$$

where d and $c_{\tau f}$ are the distance between vehicle COM to motor and coefficient for reaction torque, respectively. Considering the controller inputs as the total thrust and moments on the system, $\mathbf{u} = [f \ \mathbf{M}]^T$, the rigid body equations for SoBAR are given by:

$$\begin{aligned} \dot{\mathbf{x}} &= \mathbf{v} \\ m\dot{\mathbf{v}} &= m\mathbf{g}e_3 - f\mathbf{R}e_3 \\ \dot{\mathbf{R}} &= \mathbf{R}\hat{\boldsymbol{\Omega}} \\ J\dot{\hat{\boldsymbol{\Omega}}} &= \mathbf{M} - \hat{\boldsymbol{\Omega}} \times J\hat{\boldsymbol{\Omega}} \end{aligned} \quad (4)$$

where m denotes the vehicle mass, $\mathbf{x} \in \mathbb{R}^3$ and $\mathbf{v} \in \mathbb{R}^3$ describe the position and velocity of COM in the inertial frame, $\mathbf{R} \in \text{SO}(3)$ is the rotation matrix from the body-fixed frame to the inertial frame, $\hat{\boldsymbol{\Omega}} \in \mathbb{R}^3$ denotes the angular velocity vector in the body-fixed frame, $\mathbf{g} = 9.81\text{m/s}^2$ denotes gravity acceleration, e_3 denotes the i_3 axis unit vector and the *hat map* $\hat{\cdot} : \mathbb{R}^3 \rightarrow \text{SO}(3)$ is a symmetric matrix operator defined by the condition that $\hat{x}y = x \times y \ \forall \ x, y \in \mathbb{R}^3$.

We then use (2) and (3) to compute the individual motor thrust force (F_i) and the corresponding rotor speeds. A P-PID structure for the low-level position control loop with a geometric controller [60] for the attitude control loop is employed for SoBAR's position and attitude control.

E. Trajectory Planning for Autonomous Perching

The perching maneuver consists of multiple trajectories which are described in this section. First, SoBAR approaches the target location and localizes itself to hover 30cm above it (more details are given in Appendix E). Once the position error is within the pre-defined tolerance, SoBAR initiates the descent trajectory. The reference trajectory for the descent consists of the $x-y-z$ position setpoints. When the position errors with respect to the target perch location is approximately zero, the grasper hits the target and activates to initiate the high-impact dynamic perching. After this event, as soon as the position and velocity errors are reduced below a user defined tolerance, the propellers are turned off to remain perched. In this paper, a manual recovery is then performed by pneumatically disengaging the grasper before the take-off and landing sequence. A block diagram for autonomous perching with SoBAR is given in Fig. 4 with the perching strategy highlighted in the orange sub-block.

III. RESULTS

A. Grasper Evaluation

To characterize the performance of the HFB grasper, we first evaluated each HFB actuator for its tip force, activation force, and activation and recoil time. These experiments are detailed in Appendix F. From the tests, we decided to utilize a triple spring steel set, that generates a grasping force of 200N, tip force of 0.55N, activates within 4ms, and pneumatically recoils within 3s with a minimum input pressure of 83kPa. From the activation force tests, we were able to approximate its desired impact velocity. With an impact time of approximately 0.1s (captured by the 500-fps high-speed camera), the triple spring steel set leads to a minimum approach velocity of 2.4m/s, which corresponds to a free-fall drop height of approximately 30cm. This insight is effectively employed to demonstrate successful perching as shown in Sec. III-C.

We then designed the experiments with UTM for evaluating the grasping force of the multi-fingered grasper for perching. We tested the maximum grasping force for the two- and three-fingered actuator configurations, as seen in Fig. 6. For each configuration, experiments were conducted on three cylinder diameters (55mm, 80mm and 115mm), chosen based on various perch sizes of interests. The graspers were fixed in place, in a horizontal position, while the cylinders were pulled

impact times and peak accelerations of the frames in “+” and “x” configurations. We also evaluated the drops at two different set heights of 25cm and 50cm corresponding to two different impact velocities of 2.21m/s and 3.1m/s respectively. The impact times were captured with a high-speed camera, shown in Supplementary Video 2. The results are shown in Fig. 8A, B and C, and summarized in Table I. Figs. 8D and E, represent the experimental setup utilized and is further detailed in Appendix D. Slow motion frame captures of a single drop test for the “+” and ‘x’ configurations of the soft-bodied frame at 138kPa, are shown in Figs. 8D(i) and (ii). It is also similarly displayed for the rigid frame in Figs. 8E(i) and (ii). The rest of the drop tests are presented in Appendix H.

For the rigid frame, the impact time for the “x” and “+” configurations was approximately 22ms and 8ms. The maximum peak acceleration experienced by the frame was approximately 390m/s^2 , corresponding to a very high peak impact force of 430N, as seen in Fig. 8A. These high impact forces were experienced by the chassis because the rigid frame does not deform, transmitting the entire impact force to the main body. We hypothesize that the large variance in impact force readings is due to the impact times being so miniscule, that, at the current sampling rate of the sensor (maximum of 1kHz), it would sometimes miss the peak acceleration reading. On the other hand, the soft-bodied frame of SoBAR generated deformation upon collision, which led to much longer impact time ($10\times$ in both configurations) compared to the rigid frame. The soft-bodied frame is capable of extending the contact impact time through its body deformation, which leads to lower impact force as shown in Figs. 8B and C.

Between the “+” and “x” configurations of the soft-bodied frame, we notice that the “+” configuration experiences lower impact forces overall. Although the “x” configuration highlights longer impact times, as seen in Table I, its arms mitigate the impact by splitting outwards which can be less ideal for collision mitigation. For example, Fig. 8B highlights the experiment with the SoBAR frame that experienced the largest recorded impact forces at 138kPa and 50cm, also captured in Fig. 8Dii. We notice that at 120ms, the arms have completely split outwards, causing the chassis to impact the ground, thus leading to high impact forces. This behavior is even worse with the 69kPa frame when dropped at 50cm, saturating the on-board accelerometer. The slow motion capture of this test is highlighted in Fig. 13. This behavior is analogous to Euler springs where beyond the maximum compression distance, the entire impact force is transmitted to the chassis. However, by increasing the internal pressure of 207kPa, even at the 50cm drop, the “x” configuration is able to successfully mitigate the impact without the main chassis contacting the ground.

Since, indoor aerial robots are prone to collisions with impact velocities upto 2m/s, we chose to utilize the “+” configuration at 207kPa, to maximize the collision mitigation ability and minimum thrust loss (discussed in Sec. III-B1) for the collision and flight demonstrations with SoBAR, in Secs. III-B3 and III-C1.

3) *Collision Demonstration*: To verify SoBAR’s collision performance, we carried out a series of experiments where the drone took off and approached the target setpoint without the

TABLE I
IMPACT TIMES FOR SOBAR AND THE RIGID DJI F450 FRAME IN VARIOUS CONFIGURATIONS

Frame	Pressure	‘x’ configuration impact time (ms)		‘+’ configuration impact time (ms)	
		25cm	50cm	25cm	50cm
Rigid	-	22.1	-	8	8
Soft	69kPa	96.4	124.5	80.3	78.3
Soft	138kPa	164.7	84.3	68.3	122.5
Soft	207kPa	146.6	108.4	72.3	78.3

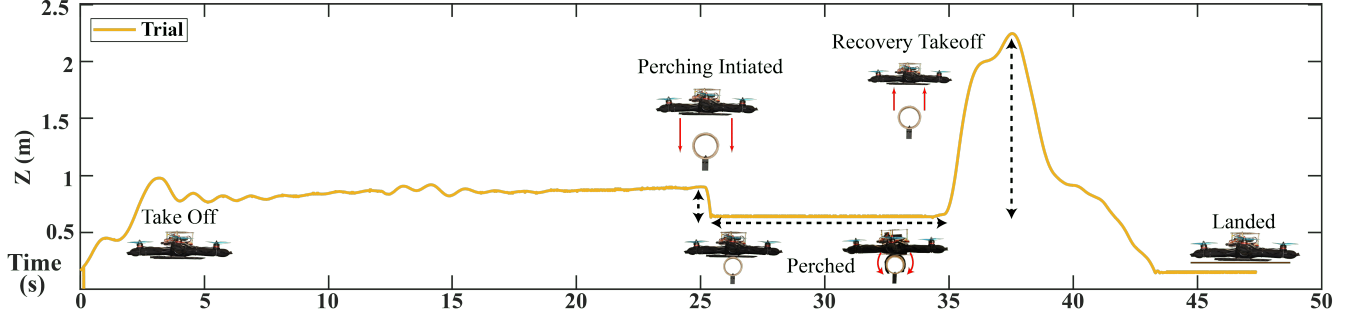
knowledge of the wall. Upon collision, it recovered and the collision trajectory was recorded in slow motion, as seen in Fig. 8F. It is seen that due to the deformation of the soft body, low rebound velocities in the range of 1.5m/s corresponding to high collision velocities of up to 2m/s are achieved. These low rebound velocities help in post-collision recovery control without the need for complex collision characterization [30]. The head-on collision performance is highlighted in Supplementary Video 4. For the conventional rigid chassis, the rebound velocities are significantly higher, as observed through our experimental tests that were also captured with the high speed camera and shown in Supplementary Video 2 and Appendix H, leading to complex collision characterization and recovery control [30].

C. Perching with SoBAR

1) *Real-time Experiments*: The z position trajectory of SoBAR for real-time perching is shown in Figs. 9A and B. This coordinate was chosen to mark the various phases of the maneuver, as shown in the Figs. 9A and B. We demonstrate SoBAR’s perching ability on a cylindrical and rectangular cross-sectioned objects, also highlighted in Supplementary Video 5. Initially, SoBAR approaches and hovers above the target location, which is obtained by placing an infrared marker on the perching object. This hover phase is marked where the height is oscillating due to small errors in the tracking control. Once the position errors fall within the preset bound, the free-fall descent is initiated for perching, this is shown by the steep slope of the z position trajectory. After the successful perch, SoBAR rests for a user defined wait time, and then performs a manual recovery and landing sequence. The perching results on the two different objects are shown in Figs. 9A and B, respectively. As previously mentioned, since the object radius is within the maximum grasp radius, we have significantly high success rates (four out of five times). Figures 9C and D, highlight snapshots of the experimental setup and the real-time perching, recovery, and landing maneuvers.

2) *Perching with Rigid vs. Soft-Bodied Frame*: We compared the perching ability between SoBAR and rigid DJI frames, mounted with the HFB grasper, dropped from a height of 25cm onto a circular perch, as seen in Figs. 9E and F, and Supplementary Video 5. For the rigid frame, we notice that the impact times are significantly smaller (2-4ms) leading to higher impact forces. These forces are too large to not only activate the grasper, but also cause a rebound motion, as shown in Fig. 9E(ii) and (iii), which causes the system to bounce off the perch, before the grasper can successfully engage, as shown in Fig. 9F(iii). As the grasper is already partially

A. Takeoff, perch, recover, and land sequence on a Circular Perch



B. Takeoff, perch, recover, and land sequence on a Rectangular Perch

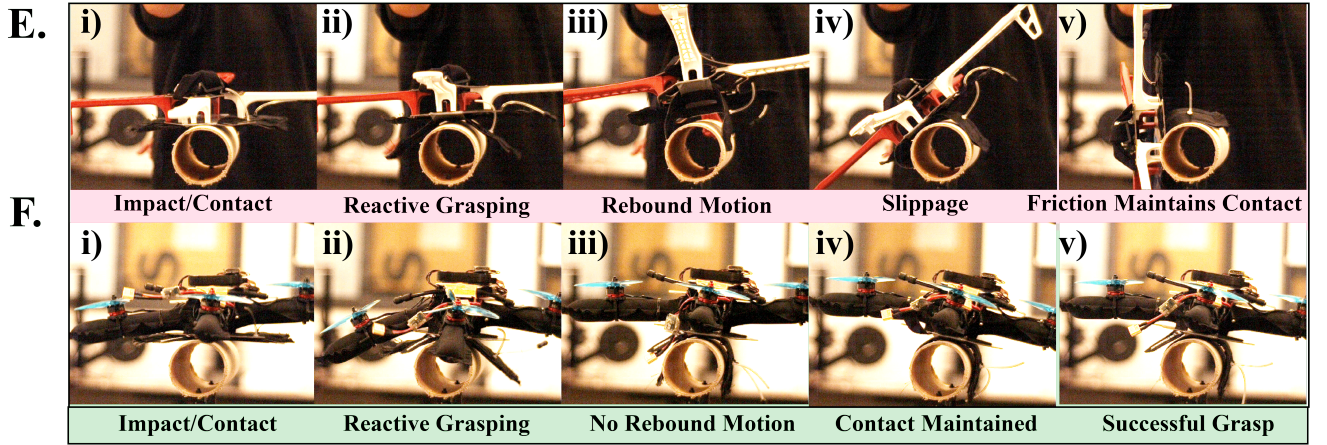
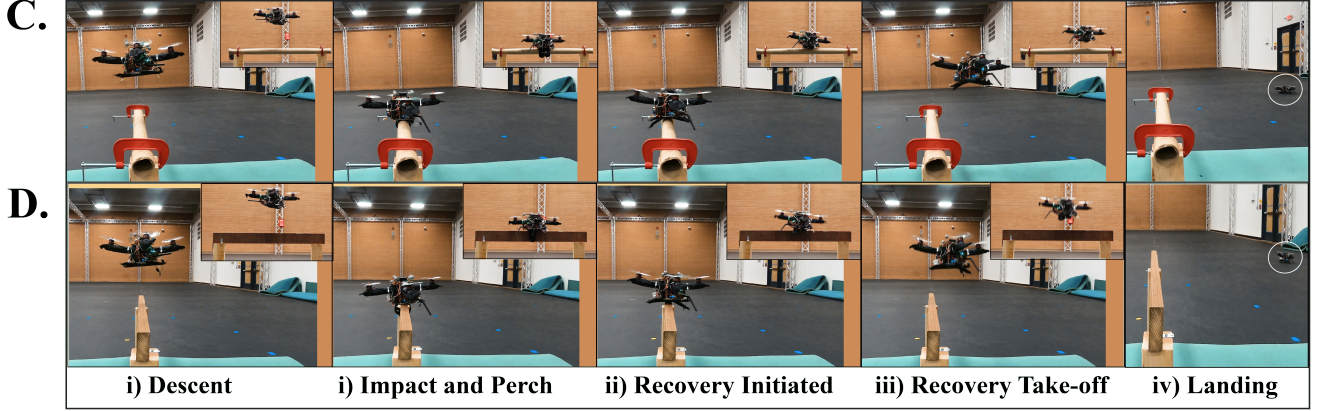
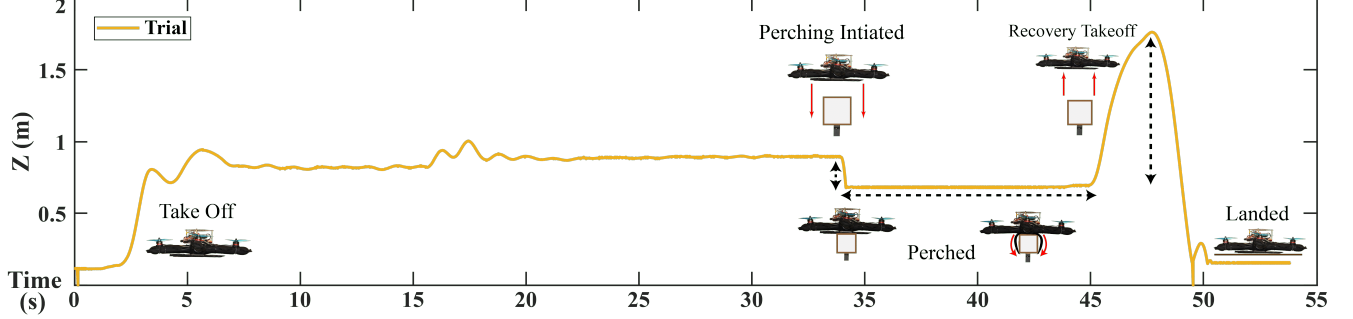


Fig. 9. Takeoff, perch, recover, and land sequence of SoBAR for one of the three successful trials. (A) Successful perching on a circular object can be inferred from SoBAR's 'z' position trajectory. (B) Successful perching on a rectangular object can be inferred from SoBAR's 'z' position trajectory. (C) Real-time perching sequence of soft-bodied aerial robot on circular perch, from front and side view. (D) Real-time perching sequence of soft-bodied aerial robot on rectangular perch, from front and side view. (E) Rigid frame with perching mechanism demonstration. Notice a large rebound motion at (ii) causing slippage in (iv). (F) Soft aerial robot with perching mechanism demonstration

activated, the friction on the fingers helps the rigid frame from completely falling off. However, because of the uneven application of wrench forces, there is noticeable slippage, seen in Fig. 9E(iv), until enough contact is reached in Fig. 9E(v). This leads to unpredictable final configurations, as shown in Fig. 9E(v) (roll angle almost 90°), which can be difficult to recover from. The success rate for this case scenario was one out of five.

With SoBAR's frame, we notice that upon impact, Fig. 9F, it undergoes deformation and increases its impact time as shown in Figs. 9F(iii) to (v). This allows contact with the perch for a longer time, leading to successful engagement of the HFB grasper. SoBAR was able to successfully perch four out of five times. This highlights how the deformable body improves the perching capabilities in comparison to the rigid frame, and aids in the application of the wrench forces, without explicit grasp hull computations and results in a robust grasp during the perching task.

IV. DISCUSSIONS AND CONCLUSION

This paper presented the design, development, and evaluation of an untethered, lightweight, robust, and compliant fabric soft-bodied aerial robot (SoBAR) composed of a soft-bodied frame and hybrid fabric-based bistable (HFB) grasper. The vision of this work was geared towards addressing two previously disconnected capabilities in aerial robots, namely, impact mitigation and dynamic perching. Towards this goal, we developed an intrinsically soft aerial frame, with embodied physical intelligence, which includes high robustness, light weight, and tunable stiffness for flight stability and collision resiliency. Equipped on the bottom of the soft-bodied frame, we developed the HFB grasper that utilizes bistability to passively switch from a landing gear (straight beam state) to a grasper (continuum curled state), maintaining both states without any additional activation but utilizes pneumatic activation to return from a curled to a straight beam state. The soft-bodied frame and the HFB grasper synergistically assist each other to perform high-speed, high-impact, and dynamic collision-based perching by mitigating the free-fall drop impact to extend the robot's contact time with the perch and support the activation of the HFB grasper within 4ms.

In particular, the soft-bodied frame design took into consideration the innate features of high-strength inflatable woven fabric beams to maintain a lightweight of 10g, while still being able to adapt its stiffness pneumatically to achieve high stiffness during flight. Yet, when completely deflated, SoBAR is completely stowable and storable. With the utilization of a soft-bodied frame, at the internal pressure of 207kPa, we experienced a beam deflection of approximately 5.80° , which affected the net thrust force and SoBAR's flight efficiency. We accounted for this by modeling the thrust coefficient as a function of this deflection angle for controller design. In the future, we can improve the overall stiffness of the frame by employing an onboard pump rated at a higher operating pressure, since the maximum burst pressure of the frame is rated at approximately 345kPa. We could also add rigid reinforcements at the joints of the frame's arms to limit the deflections.

We demonstrated the soft-bodied frame's ability to mitigate impact from head-on collision with a series of comparative drop tests. We noticed vastly improved collision mitigation abilities, in both plus and cross configurations. In the future, we will develop a stiffness model for the soft-bodied frame as a function of the internal pressure that generates the desired stiffness for collision resilience based on the robot's approach velocity during head-on collision. We also demonstrated a successful recovery of the SoBAR from head-on collisions at a speed up to 2m/s. We noticed that after numerous collision tests, the motor mounts on the arms of SoBAR, seen in Fig. 2A(ii) had to be readjusted due to minor slippage. This might be addressed by adding anti-slip fabric at the interface between the motor mount and the fabric frame. In addition, we could also sew the motor mounts directly on the fabric frame, with minor sacrifice of stowability.

The design considerations taken for the HFB grasper included its speed of grasp, shape of grasp, payload capacity, and passive contact-reactive nature. For the successful implementation of the HFB grasper, we developed a system that did not require active control based on the timing of the robot's perching performance, but instead, reacts instantly upon contact with the perch. The contact-reactive grasper converts the impact energy to rapidly switch states in less than 4ms. Its shape conforming nature enables it to adapt to unknown surface geometries and textures, demonstrated with the cylindrical pipe and rectangular prism log in this work. The grasper demonstrates grasping forces of up to 200N, around a 55mm circular perch, which is more than 500% its own weight. The grasping payload of the system is related to the number of bistable spring steels utilized, which was three in this work. The limitation of scaling up the number of spring steels directly correlates to the minimum approach speed of the robot, which was theoretically calculated and then characterized as a downward velocity of 2.4m/s or a free-fall drop of 30cm. To adjust the drop height of the system, the rotors can be activated to generate a desired downward velocity. Finally, to study the integrated dynamic perching mechanism, we also performed various characterization tests of the grasper and its components, modeled and analyzed the grasping wrench on objects with a circular and rectangular cross sections, and demonstrated a full control pipeline of SoBAR (from perching, recovering, and landing) in a controlled indoor environment.

From our free-fall drop perching experiments, we noticed that depending on its last position before the rotors are turned off and its landing contact position, SoBAR does not always land dead center, and could lean slightly to the right or to the left. We hypothesize that the perching accuracy is related to the minor position errors of SoBAR during hovering, right before its free-fall drop, as well as minor slippage due to the friction contact and the dynamics of the grasper upon impact with the perch, usually when it experiences a small rebound motion. Future work will look to further understand the grasper through additional characterization of its torsional stability.

With SoBAR, we look forward to exploring its perching capabilities with variable sized and highly textured perchable objects, such as tree branches, and compliant and inclined perches as well. We will also look to implement control

and perception strategies for autonomous outdoor perching capabilities by visually detecting suitable perches. Future work, will also involve in-depth investigations on the energy efficiency and flight aerodynamics of SoBAR in comparison to conventional multirotor aerial vehicles, during flight. All these future effort will enable long outdoor monitoring, search, and data collection missions.

ACKNOWLEDGEMENT

We would like to thank Saivimal Sridar, Weijia Tao, YiZhuang Garrad, and Sunny Amatya for their help with fabrication, setting up video recordings, setting up the UR5 tests, and helpful suggestions during the ideation and paper editing process. We would also like to thank Prof. Panagiotis Polygerinos for the brainstorming and stimulating discussions on this topic.

REFERENCES

- [1] T. W. Danko, A. Kellas, and P. Y. Oh, "Robotic rotorcraft and perch-and-stare: sensing landing zones and handling obscurants," in *ICAR '05. Proceedings., 12th International Conference on Advanced Robotics, 2005.*, pp. 296–302, 2005.
- [2] M. Kovač, J. Germann, C. Hürzeler, R. Y. Siegwart, and D. Floreano, "A perching mechanism for micro aerial vehicles," *Journal of Micro-Nano Mechatronics*, vol. 5, no. 3, pp. 77–91, 2009.
- [3] M. Graule, P. Chirarattananon, S. Fuller, N. Jafferis, K. Ma, M. Spenko, R. Kornbluh, and R. Wood, "Perching and takeoff of a robotic insect on overhangs using switchable electrostatic adhesion," *Science*, vol. 352, no. 6288, pp. 978–982, 2016.
- [4] J. Thomas, M. Pope, G. Loianno, E. W. Hawkes, M. A. Estrada, H. Jiang, M. R. Cutkosky, and V. Kumar, "Aggressive Flight With Quadrotors for Perching on Inclined Surfaces," *Journal of Mechanisms and Robotics*, vol. 8, no. 5, p. 051007, 2016.
- [5] L. Daler, A. Klapotcz, A. Briod, M. Sitti, and D. Floreano, "A perching mechanism for flying robots using a fibre-based adhesive," in *2013 IEEE International Conference on Robotics and Automation*, pp. 4433–4438, IEEE, 2013.
- [6] M. T. Pope, C. W. Kimes, H. Jiang, E. W. Hawkes, M. A. Estrada, C. F. Kerst, W. R. Roderick, A. K. Han, D. L. Christensen, and M. R. Cutkosky, "A Multimodal Robot for Perching and Climbing on Vertical Outdoor Surfaces," *IEEE Transactions on Robotics*, vol. 33, no. 1, pp. 38–48, 2017.
- [7] K. Zhang, P. Chermprayong, T. M. Alhinai, R. Siddall, and M. Kovac, "Spidermav: Perching and stabilizing micro aerial vehicles with bio-inspired tensile anchoring systems," in *2017 IEEE/RSJ International Conference on Intelligent Robots and Systems (IROS)*, pp. 6849–6854, 2017.
- [8] H.-N. Nguyen, R. Siddall, B. Stephens, A. Navarro-Rubio, and M. Kovač, "A passively adaptive microspine grapple for robust, controllable perching," in *2019 2nd IEEE International Conference on Soft Robotics (RoboSoft)*, pp. 80–87, IEEE, 2019.
- [9] M. Kovač, J. Germann, C. Hürzeler, R. Y. Siegwart, and D. Floreano, "A perching mechanism for micro aerial vehicles," *Journal of Micro-Nano Mechatronics*, vol. 5, no. 3-4, pp. 77–91, 2009.
- [10] W. R. Roderick, H. Jiang, S. Wang, D. Lentink, and M. R. Cutkosky, "Bioinspired grippers for natural curved surface perching," in *Conference on Biomimetic and Biohybrid Systems*, pp. 604–610, Springer, 2017.
- [11] Z. Zhang, P. Xie, and O. Ma, "Bio-inspired trajectory generation for uav perching," in *2013 IEEE/ASME International Conference on Advanced Intelligent Mechatronics*, pp. 997–1002, IEEE, 2013.
- [12] C. E. Doyle, J. J. Bird, T. A. Isom, J. C. Kallman, D. F. Bareiss, D. J. Dunlop, R. J. King, J. J. Abbott, and M. A. Minor, "An avian-inspired passive mechanism for quadrotor perching," *IEEE/ASME Transactions on Mechatronics*, vol. 18, no. 2, pp. 506–517, 2013.
- [13] M. A. Erbil, S. D. Prior, and A. J. Keane, "Design optimisation of a reconfigurable perching element for vertical take-off and landing unmanned aerial vehicles," *International Journal of Micro Air Vehicles*, vol. 5, no. 3, pp. 207–228, 2013.
- [14] W. Chi, K. H. Low, K. H. Hoon, and J. Tang, "An optimized perching mechanism for autonomous perching with a quadrotor," in *IEEE International Conference on Robotics and Automation*, pp. 3109–3115, 2014.
- [15] W. Roderick, M. Cutkosky, and D. Lentink, "Bird-inspired dynamic grasping and perching in arboreal environments," *Science Robotics*, vol. 6, no. 61, p. eabj7562, 2021.
- [16] S. Kirchgeorg and S. Mintchev, "Hedgehog: Drone perching on tree branches with high-friction origami spines," *IEEE Robotics and Automation Letters*, 2021.
- [17] M. Sitti, "Physical intelligence as a new paradigm," *Extreme Mechanics Letters*, vol. 46, p. 101340, 2021.
- [18] R. Cory and R. Tedrake, "Experiments in fixed-wing UAV perching," *AIAA Guidance, Navigation and Control Conference and Exhibit*, pp. 1–12, 2008.
- [19] J. Moore and R. Tedrake, "Control synthesis and verification for a perching uav using lqr-trees," in *2012 IEEE 51st IEEE Conference on Decision and Control (CDC)*, pp. 3707–3714, IEEE, 2012.
- [20] J. Thomas, G. Loianno, M. Pope, E. W. Hawkes, M. A. Estrada, H. Jiang, M. R. Cutkosky, and V. Kumar, "Planning and control of aggressive maneuvers for perching on inclined and vertical surfaces," in *International Design Engineering Technical Conferences and Computers and Information in Engineering Conference*, vol. 57144, p. V05CT08A012, American Society of Mechanical Engineers, 2015.
- [21] M. Watson, "The mechanism of perching in birds," *Journal of anatomy and physiology*, vol. 3, no. Pt 2, p. 379, 1869.
- [22] W. Chi, K. H. Low, K. H. Hoon, and J. Tang, "An optimized perching mechanism for autonomous perching with a quadrotor," in *2014 IEEE International Conference on Robotics and Automation (ICRA)*, pp. 3109–3115, 2014.
- [23] T. H. Quinn and J. J. Baume, "The digital tendon locking mechanism of the avian foot (aves)," *Zoomorphology*, vol. 109, pp. 281–293, July 1990.
- [24] W. G. Hyzer, "Flight behavior of a fly alighting on a ceiling," *Science*, vol. 137, no. 3530, pp. 609–610, 1962.
- [25] J. Thomas, G. Loianno, J. Polin, K. Sreenath, and V. Kumar, "Toward autonomous avian-inspired grasping for micro aerial vehicles," *Bioinspiration & biomimetics*, vol. 9, no. 2, p. 025010, 2014.
- [26] H. Sedaghat-Pisheh, A. R. Rivera, S. Biaz, and R. Chapman, "Collision avoidance algorithms for unmanned aerial vehicles using computer vision," *Journal of Computing Sciences in Colleges*, vol. 33, no. 2, pp. 191–197, 2017.
- [27] I. Spasojevic, V. Murali, and S. Karaman, "Perception-aware time optimal path parameterization for quadrotors," in *2020 IEEE International Conference on Robotics and Automation (ICRA)*, pp. 3213–3219, IEEE, 2020.
- [28] S. Mintchev, S. de Rivaz, and D. Floreano, "Insect-Inspired Mechanical Resilience for Multicopters," *IEEE Robotics and Automation Letters*, 2017.
- [29] L. Dilaveroğlu and O. Özcan, "Minicore: A miniature, foldable, collision resilient quadcopter," in *2020 3rd IEEE International Conference on Soft Robotics (RoboSoft)*, pp. 176–181, IEEE, 2020.
- [30] K. Patnaik, S. Mishra, Z. Chase, and W. Zhang, "Collision recovery control of a foldable quadrotor," *IEEE/ASME International Conference on Advanced Intelligent Mechatronics (AIM)*, pp. 418–423, 2021.
- [31] K. Patnaik, S. Mishra, S. M. R. Sorkhabadi, and W. Zhang, "Design and control of squeeze: A spring-augmented quadrotor for interactions with the environment to squeeze-and-fly," in *2020 IEEE/RSJ International Conference on Intelligent Robots and Systems (IROS)*, pp. 1364–1370, IEEE, 2020.
- [32] S. Coyle, C. Majidi, P. LeDuc, and K. J. Hsia, "Bio-inspired soft robotics: Material selection, actuation, and design," *Extreme Mechanics Letters*, vol. 22, pp. 51 – 59, 2018.
- [33] D. Rus and M. T. Tolley, "Design, fabrication and control of soft robots," *Nature*, vol. 521, no. 7553, pp. 467–475, 2015.
- [34] C. Laschi, B. Mazzolai, and M. Cianchetti, "Soft robotics: Technologies and systems pushing the boundaries of robot abilities," *Science Robotics*, vol. 1, no. 1, p. eaah3690, 2016.
- [35] D. Floreano and R. J. Wood, "Science, technology and the future of small autonomous drones," *Nature*, vol. 521, no. 7553, pp. 460–466, 2015.
- [36] S. Mintchev and D. Floreano, "Adaptive Morphology," *IEEE Robotics and Automation Magazine*, no. 23, pp. 42–54, 2016.
- [37] M. Di Luca, S. Mintchev, G. Heitz, F. Noca, and D. Floreano, "Bio-inspired morphing wings for extended flight envelope and roll control of small drones," *Interface focus*, vol. 7, no. 1, p. 20160092, 2017.

- [38] L. Daler, S. Mintchev, C. Stefanini, and D. Floreano, "A bioinspired multi-modal flying and walking robot," *Bioinspiration & biomimetics*, vol. 10, no. 1, p. 016005, 2015.
- [39] N. T. Jafferis, E. F. Helbling, M. Karpelson, and R. J. Wood, "Untethered flight of an insect-sized flapping-wing microscale aerial vehicle," *Nature*, vol. 570, no. 7762, pp. 491–495, 2019.
- [40] D. Q. Nguyen, G. Loianno, *et al.*, "Towards design of a deformable propeller for drone safety," in *2020 3rd IEEE International Conference on Soft Robotics (RoboSoft)*, pp. 464–469, IEEE, 2020.
- [41] J. Shintake, S. Rosset, B. E. Schubert, D. Floreano, and H. R. Shea, "A foldable antagonistic actuator," *IEEE/ASME Transactions on Mechatronics*, vol. 20, no. 5, pp. 1997–2008, 2015.
- [42] A. Tonazzini, S. Mintchev, B. Schubert, B. Mazzolai, J. Shintake, and D. Floreano, "Variable stiffness fiber with self-healing capability," *Advanced Materials*, vol. 28, no. 46, pp. 10142–10148, 2016.
- [43] P. Sareh, P. Chermprayong, M. Emmanuelli, H. Nadeem, and M. Kovac, "Rotorigami : A rotary origami protective system for robotic rotorcraft," *Science Robotics*, vol. 5228, no. September, pp. 1–13, 2018.
- [44] A. Ramezani, S.-J. Chung, and S. Hutchinson, "A biomimetic robotic platform to study flight specializations of bats," *Science Robotics*, vol. 2, no. 3, pp. Art–No, 2017.
- [45] S. J. Kim, D.-Y. Lee, G.-P. Jung, and K.-J. Cho, "Bioinspired dual-stiffness origami," *Science Robotics*, vol. 0275, no. July, pp. 1–8, 2018.
- [46] S.-J. Kim, D.-Y. Lee, G.-P. Jung, and K.-J. Cho, "An origami-inspired, self-locking robotic arm that can be folded flat," *Science Robotics*, vol. 3, no. 16, p. eaar2915, 2018.
- [47] G. Miron, B. Bédard, and J.-S. Plante, "Sleeved bending actuators for soft grippers: A durable solution for high force-to-weight applications," *Actuators*, vol. 7, no. 3, p. 40, 2018.
- [48] D.-J. Lee and G.-P. Jung, "Snatcher: A highly mobile chameleon-inspired shooting and rapidly retracting manipulator," *IEEE Robotics and Automation Letters*, vol. 5, no. 4, pp. 6097–6104, 2020.
- [49] H. Li, J. Yao, C. Wei, P. Zhou, Y. Xu, and Y. Zhao, "An untethered soft robotic gripper with high payload-to-weight ratio," *Mechanism and Machine Theory*, vol. 158, p. 104226, 2021.
- [50] M. Kovac, "Learning from nature how to land aerial robots," *Science Robotics*, vol. 352, no. 6288, pp. 895–6, 2016.
- [51] K. Zhang, Y. Zhu, C. Lou, P. Zheng, and M. Kovac, "A design and fabrication approach for pneumatic soft robotic arms using 3D printed origami skeletons," *RoboSoft 2019 - 2019 IEEE International Conference on Soft Robotics*, pp. 821–827, 2019.
- [52] F. J. G. Rubiales, P. R. Soria, B. C. Arrue, and A. Ollero, "Soft-tentacle gripper for pipe crawling to inspect industrial facilities using UAVs," *Sensors*, vol. 21, p. 4142, June 2021.
- [53] J. Fishman, S. Ubellacker, N. Hughes, and L. Carlone, "Dynamic grasping with a "soft" drone: From theory to practice," 2021.
- [54] T. N. Sullivan, B. Wang, H. D. Espinosa, and M. A. Meyers, "Extreme lightweight structures: avian feathers and bones," *Materials Today*, vol. 20, no. 7, pp. 377–391, 2017.
- [55] E. Novitskaya, C. J. Ruestes, M. Porter, V. Lubarda, M. A. Meyers, and J. McKittrick, "Reinforcements in avian wing bones: Experiments, analysis, and modeling," *Journal of the mechanical behavior of biomedical materials*, vol. 76, pp. 85–96, 2017.
- [56] P. H. Nguyen and W. Zhang, "Design and computational modeling of fabric soft pneumatic actuators for wearable assistive devices," *Scientific reports*, vol. 10, no. 1, pp. 1–13, 2020.
- [57] S. Sridar, P. H. Nguyen, M. Zhu, Q. P. Lam, and P. Polygerinos, "Development of a soft-inflatable exosuit for knee rehabilitation," in *2017 IEEE/RSJ International Conference on Intelligent Robots and Systems (IROS)*, pp. 3722–3727, IEEE, 2017.
- [58] S. Sridar, Z. Qiao, N. Muthukrishnan, W. Zhang, and P. Polygerinos, "A soft-inflatable exosuit for knee rehabilitation: Assisting swing phase during walking," *Frontiers in Robotics and AI*, vol. 5, p. 44, 2018.
- [59] C. Wielgosz, J. Thomas, and A. Le Van, "Mechanics of inflatable fabric beams," in *International Conference on Computational & Experimental Engineering and Sciences Honolulu, Hawaii, USA*, 2008.
- [60] T. Lee, M. Leok, and N. H. McClamroch, "Geometric tracking control of a quadrotor uav on se (3)," in *49th IEEE conference on decision and control (CDC)*, pp. 5420–5425, IEEE, 2010.

APPENDIX A SETTING UP SoBAR

As the robot is highly portable, the process of integrating the system starts by slotting the soft body pneumatic frame through a metal chassis, as seen in Fig. 10B(i). The metal chassis also accommodates the HFB grasper. The body is inflated mid-way to fill out the chassis and the motor-propeller holders are inserted on each arm and adjusted, shown in Fig. 10B(ii). After adjustment, the soft body is completely inflated, the power is connected, and ready for flight, highlighted in Fig. 10B(iv) and (v). The process to setup SoBAR takes approximately 4min, as is demonstrated in Supplementary Video 1.

APPENDIX B FABRICATION OF SoBAR FRAME AND HFB GRASPER

A unibody structure was employed to fabricate SoBAR's frame, as seen in Fig. 2A. The nylon fabric, parchment paper, and TPU material (DT-2001, American Polyfilm, Branford, CT) were first cut into the desired morphology using the laser-cutter (Glowforge Prof, Glowforge, Seattle, WA), shown in Fig. 2A(i). The TPU bladder was made by aligning two TPU sheet cut-outs, sandwiching the parchment paper cut-out in the middle, and heat-sealed utilizing the (FLHP 3802, FancierStudio, Hayward, CA), at 275°F for 45s. The pneumatic fitting (5463K361, McMaster-Carr, Elmhurst, IL) was also added in the TPU bladder. The two sheets of nylon fabrics were sewn along the edges, utilizing a super-imposed seam, and the complete TPU bladder was inserted in the middle of the prepared nylon fabric shell, to complete SoBAR's frame, as seen in Fig. 2A(ii).

In order to fabricate these HFB actuators, we wanted to utilize a lightweight bistable material that would maintain a straight beam state but also is capable of switching to a curled state upon contact with the perch, inspired by the snap-bracelets seen in kid's toys. To utilize a low-cost off-the-shelf solution, we chose the bistable metallic tape-spring, that would allow us to scale the length of the actuator as well as its thickness, by stacking multiple tape-springs. We first cut the measuring tape (STANLEY STA030696N, Amazon.com Inc., Seattle, WA) to the desired size, seen in Fig. 2B(i). We also chamfered the edges for safety. The bistable metal has two sides, with one being concave and the other convex. To pre-form the spring steel, we rolled and bent it tightly along the convex side, around a cylindrical object. The tightly curled spring steel was wrapped to maintain shape, for 30min, as shown in Fig. 2B(ii). The spring steel was then able to switch between two states: (i) straight beam (ii) curled state, in Fig. 2B(iii).

The TPU material, parchment paper, nylon fabric, and 210D TPU-coated nylon fabric (DIY Packraft Ltd., Smithers, BC), were cut utilizing a laser cutter, as in Fig. 2B(iv). A TPU actuator was manufactured in order to perform recoil after perching. Three pre-formed tape spring steels were aligned and sandwiched between the TPU-coated nylon sheets, and heat-sealed with the heat press, to make the spring steel set, shown in Fig. 2B(iv). A pouch was then made utilizing nylon fabric,

TABLE II
MASS BUDGET OF SoBAR

Unit	Weight (g)	Total Weight Percentage (%)
Soft-bodied frame	10	0.9
4 × (motor and propeller pair)	126	11
Micro diaphragm pump	100	8.8
4S LiPo battery	250	22
Chassis	81	7.1
4 × (motor mounts)	28	11.3
Flight controller	50	4.4
Intel UP board	100	8.8
2 × (grasper fingers)	76	6.7
Grasper mount	39	3.4
Other electronics (power supply, BEC mo. *dules, voltage regulator, wifi module etc.) other (miscellaneous)	177	15.6

by sewing the edges and the TPU actuator and spring steel set were inserted in the pouch. Finally, the bottom surfaces of each grasping actuator were equipped with high-friction grip material (3M TB614, 3M Company, Maplewood, MN), completing the fabrication of the HFB actuator. Each completed actuator weighs only 38g. The multi-fingered perching mechanism can be designed in different orientations, as in Fig. 2A(iv). In this work, we only tested the two-fingered and three-fingered configurations for the soft-bodied aerial robot, as depicted in Fig. 2A(iii).

APPENDIX C

ELECTRONICS, MASS BUDGET AND INTEGRATION

SoBAR's chassis hosts the flight controller, power module, and high level controller, as seen in Fig. 3. Flight controller utilized is a PIXHAWK flight controller with the Intel UP Board as the companion computer. The high-level companion computer is used to relay the position and orientation data from the indoor motion capture system to the flight controller at 120 Hz for objects of interest within the flight arena (SoBAR and the perching objects). Analog pressure sensors (ASDX-AVX100PGAA5, Honeywell International Inc., Morris Plains, NJ) and a micro diaphragm pump (NMP830 HP-KPDC-B) are used to control the pressure of the body and the HFB actuator. The PIXHAWK flight controller is modified from the off-the-shelf code in order to integrate the micro-pump, its controller, and control allocation. The onboard micro-pump is connected to the soft grasper and body frame. In this work, the soft-bodied frame is inflated up to 207kPa and evaluated at intervals of 69kPa. To fully recoil the soft grasper only 83kPa is required. The flight control unit connects to the pressure sensor and micro-pump using I²C and Analog-Digital (AD) interfaces respectively. A standard proportional controller is implemented to control the pressure output from the micro-pump. 4S lithium polymer battery of 3300 mAh LiPo battery of 14.8V, 50C is used for the power supply. The motors are controlled utilizing Lumenier 30A BLHeli_S Electronic Speed Controllers (ESCs) and the entire system has a maximum thrust-to-weight ratio of 4.58:1. The mass budget of the system is highlighted in Table II. Noticeably, the soft robotic components and their mounting brackets make up only 19.7% of the entire system. Overall, SoBAR has a size of 319×319mm and weighs 1.14kg.

APPENDIX D EXPERIMENTAL SETUP

To characterize the HFB actuators and SoBAR's deflection, a universal tensile testing machine (UTM) (Instron 5944, Instron Corp., High Wycombe, United Kingdom) was utilized. To monitor the collision and drop tests, and the HFB actuator activation time, a 500fps high-speed camera (Edgetronics SC1, CA, USA) was utilized. To set up the drop tests, the frames were mounted on the UR5 robot manipulator, with a controlled Hand-E grasper (Universal Robotics, Odense, Denmark). To monitor the peak impact accelerations of the drop tests, a high-G accelerometer SparkFun H3LIS331DL (Sparkfun, Boulder, Colorado), with a maximum reading of 400G, was utilized. The sensor was capable of measuring acceleration at 1kHz sampling rate. Finally, the indoor perching experiments were performed utilizing a Vicon motion capture system (OptiTrack, NaturalPoint, Inc., Corvallis, OR) to obtain the position and orientation information of SoBAR and the perching location. SoBAR's soft-bodied frame's stiffness was varied by modifying the internal pressure increments of 69kPa, from 69kPa up to 207kPa, throughout the experiments.

APPENDIX E

PERCHING TASK PLANNING

Due to the complexities in autonomous recovery control and due to the scope of this paper, we present autonomous perching with a manual recovery control, leaving autonomous recovery for future work.

The entire perching maneuver consists of multiple control strategies which are described in this section. The first trajectory involves a maneuver where SoBAR's flies to the perching location to hover till the error in position is near zero and descends over the perching target with a specified downward velocity. This velocity is computed from a drop test by iterating over the height h which engages the grasper to achieve a successful perch. This also corresponds to the activation force (as computed in Sec. III-A3) for a impact time of about 0.1s. Neglecting air resistance for low velocities, the impact velocity is calculated using

$$v_t = \sqrt{2gh} \quad (5)$$

where v_t is the impact velocity and g is the constant for acceleration and h is the height from which the platform is dropped. We see that, for the current system weight, the impact force generated by a free fall from a height of 30 cm is effective to engage the grasper successfully and the corresponding impact velocity is approximately 2.4m/s. The reference trajectory for the downward descent are therefore chosen as the x-y coordinates of the perching target and the z-direction velocity for the cascaded P-PID low level position controller. The perching maneuver strategy is shown in the orange colored sub-block of the block diagram in Fig. 4.

APPENDIX F

SINGLE HFB ACTUATOR EVALUATION

A. Single Actuator Activation and Recovery Time

In this test, we evaluated the time taken for each finger to go from a straight beam state to a curled state (activation) and

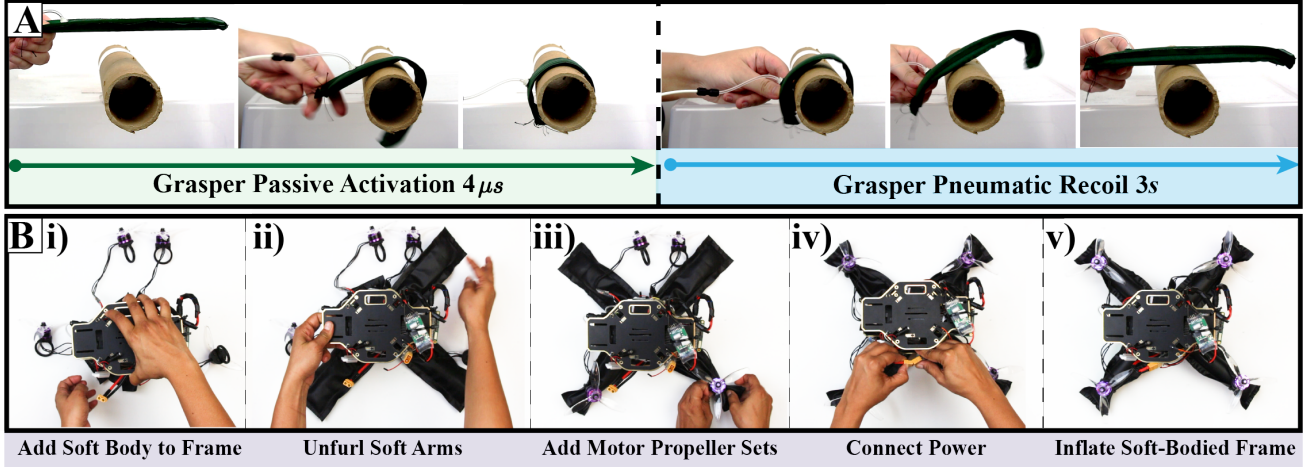


Fig. 10. (A) Grasping sequence of actuator (B) Setting up and assembling SoBAR, approximately 4mins taken.

pneumatically recover the actuator from the curled state back to its initial state, as shown in Figs. 1B and 10A. To do so, we tracked the time sequence using a high-speed camera at 500fps. We set the pressure to recoil back to a straight beam state at 83kPa, which is the minimum pressure required to recoil from prior trial-and-error testing. From the high-speed footage, we measured the activation stage to take only 4ms and the pneumatically actuated recovery stage to take 3s. This is highlighted in the Supplementary Video 2 as well.

B. Single Actuator Tip Force

A single HFB actuator was utilized to evaluate the actuator tip force, using the UTM. The finger's tip is placed in contact with the UTM's load cell. The finger is then activated at the proximal end, and the tip force is measured. The actuator tip force with a single spring steel is 0.16N and that with three embedded spring steels is 0.55N.

C. Single Actuator Activation Force

To evaluate the force required to activate a single actuator (the activation force required for the actuator to switch from a straight beam state to a completely curled state), we aligned a single actuator underneath the load cell of the UTM, with the convex side up. The UTM was designed to push downwards at a rate of 8mm/s until the activation force is recorded. The activation force of 7N, 24N, and 54N was recorded for an actuator with a single, triple, and quintuple embedded spring steels, respectively.

From the activation force, we are able to calculate the approximate desired impact velocity. The impact time is approximately 0.1s as visualized by the high-speed camera, leading to impact velocities of 0.7m/s, 2.4m/s, and 5.4m/s in the body z direction of SoBAR, for the single, triple, and quintuple embedded spring steels graspers, respectively. For real-world experiments, we decided to utilize the grasper with three embedded spring steels by optimizing the three parameters of required impact velocity, achieved grasp force and total weight addition by the grasper.

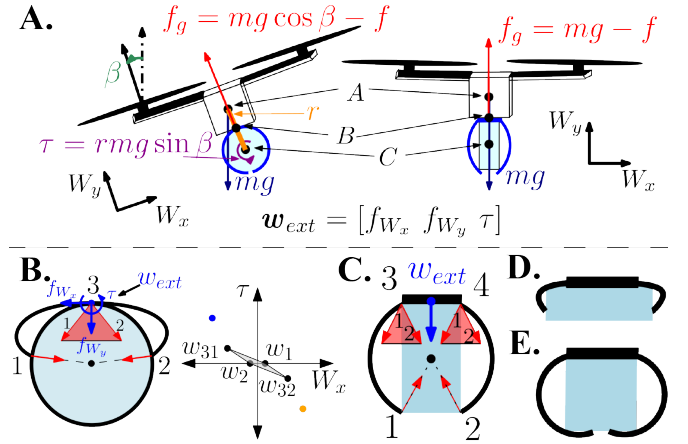


Fig. 11. Modeling the various features of SoBAR for perching and flying conventionally. (A) External wrench for circular and square objects. (B) Wrench hull for circular object larger than the grasp radius. (C) Grasp consisting of one friction force and two frictionless point forces (D) Perching on a side larger than grasp radius (E) Perching on an object within the grasp radius.

APPENDIX G

STATIC WRNCH ANALYSIS OF THE GRASPER FOR NON-CONFORMABLE OBJECTS

We perform a static grasp wrench analysis to obtain an insight into whether SoBAR with the HFB grasper will successfully perch on objects, with shapes and sizes, that do not conform to the grasper workspace. For the wrench analysis, we assume a 2D object and the wrench space in \mathbb{R}^3 , neglecting any movement in longitudinal direction of the perching object.

Figure 11A illustrates the external wrench on the grasper in different scenarios (objects with circular and rectangular cross-sections) and the reference wrench frame, W , which is located at the center of the grasper and oriented with the body z axis of SoBAR's. The gravitational force (mg) acting on SoBAR's center of gravity (Point A) and the reaction force (f_g) acting at the point of contact (Point B) is transferred to Point C, the center of the object. Note that the reaction force compensates for any residual thrust from the motors, denoted in the figure by f . For the circular cross-section, there is an

acting torque at Point C due to the perch orientation but for the rectangular cross-section, the external wrench will only consist of the contact forces and gravitational forces, excluding any torques, due to the flat surface on which SoBAR perches. In order to ensure a successful perching, the maximum force by the grasper should be able to generate an equal wrench in the opposite direction. For the analysis that follows, the friction coefficient, μ , between the high-friction grip material used on the grasper and the cardboard material of the perching object is taken as 0.7 as calculated from experiments.

We first consider a scenario where SoBAR's perches on a circular object with a diameter (115mm) greater than the workspace of the two-finger grasper (70mm). With the values

$$m = 1.14\text{kg}, \beta = 30^\circ, g = 9.81\text{m/s}^2,$$

and

$$r = r_{AB} + r_{BC} = \left(50 + \frac{115}{2}\right)\text{mm} = 107.5\text{mm},$$

we can calculate the components of the external wrench, w_{ext} , as:

$$f_{W_x} = -mg \sin \beta = -5.59\text{N}$$

,

$$0 \leq f_{W_y} \leq (mg \cos \beta - f)$$

and

$$\tau = 0.6\text{Nm},$$

where f is residual thrust during perching and is significantly less than mg . To compute the grasp wrench hull, we can assume that there are three forces as shown in the free body diagram of Fig. 11B. The forces are approximated as follows - a friction cone at point "3" and two frictionless point forces at locations "1" and "2" respectively which are directed towards the center of the object. To account for the curled tip force that is not exactly directed towards the center, we approximate a loss cone of $\pm 5^\circ$ within which the tip force lies. Depending on the grasp wrench hull, we will be able to tell if the external wrench (shown by the blue dot in Fig. 11B) can be compensated by the grasper in the configuration for a large object as shown in Fig. 11B. With the above-mentioned parameters, we obtain:

$$f_{g_{max}} = mg \cos \beta = 9.68$$

Using the tip force values as calculated from experiments and neglecting the small torque generated by these forces:

$$f_1 = -f_2 = 0.55\text{N},$$

and

$$f_{31} = -f_{32} = \mu f_{g_{max}} = 6.78\text{N}$$

with a friction cone of angle

$$\alpha = \tanh \mu = 35^\circ$$

We can now calculate the wrench generated by the grasper as

$$w_1 = [0.54 \ -0.1 \ 0]^T,$$

$$w_2 = [-0.54 \ -0.1 \ 0]^T,$$

$$\begin{aligned} w_{31} &= [-f_{31} \sin \alpha \ f_{31} \cos \alpha \ r_{BC} f_{31} \sin \alpha]^T \\ &= [-3.88 \ -5.55 \ 0.22]^T \end{aligned}$$

and similarly

$$w_{32} = [3.88 \ -5.55 \ -0.22]^T$$

We can infer that no linear combination of the grasper forces can cancel out the external wrench. As shown in the Fig. 11B, the required wrench (the yellow dot) falls outside the wrench hull in this case, and hence leads to an unstable perch. This is accounted by the fact that the grasper cannot generate required force and torque in this configuration to cancel out the external wrench's component in W_x direction and τ .

We proceed in a similar way to model the grasp wrench for one narrow side rectangular object which lies within the grasp radius (20mm×40mm). Here, we consider a total of four forces - two friction cones at the two top corners as shown in Fig. 11C and two frictionless point forces at the tip of either end of the grasper. In this case however, there is no external torque acting after the perching maneuver and the ground reaction force helps counter the gravitational forces on the body. With the aforementioned parameters and assuming that all the tip forces at 1 and 2 act towards the center of the object, as shown in the figure, we can compute each wrench force as mentioned in previous section. Specifically, the forces are calculated to be

$$f_1 = [0.26\sqrt{2} \ 0.26\sqrt{2}]^T,$$

$$f_2 = [-0.26\sqrt{2} \ 0.26\sqrt{2}]^T,$$

$$f_{31} = f_{41} = [-4.49 \ -6.41]^T,$$

$$f_{32} = f_{42} = [4.49 \ -6.41]^T$$

The grasper can resist small arbitrary forces in this configuration since the origin lies within the wrench hull. Note that, if the object is larger than the grasp radius, as shown in Fig. 11D, the ground reaction force can help stabilize SoBAR's-grasper system after perching, given a flat final orientation. For objects that do not conform to the size but lie within the grasp radius, Fig. 11E, the grasper can effectively generate forces to hold on to the perch and resist take-off. This configuration can be modelled as four friction forces, two at the top point of contact and two friction forces at the bottom pints of contact which ensures that the configuration is in force closure. This phenomena is clearly demonstrated in Supplementary Video 5. We successfully employ these insights to demonstrate real-time experiments with SoBAR on objects that ensure successful perches, seen in Sec. III-C.

APPENDIX H COLLISION DROP TESTS

In this section, we present the rest of the slow motion screen captures for the collision drop tests that were not shown in Fig. 8.

The drop tests for the soft-bodied frame at 69kPa are shown in Figs. 12 and 13. The drop tests for the soft-bodied frame at 138kPa are highlighted in Figs. 14 and 15. Finally, the drop tests for the soft-bodied frame at 207kPa are presented in Figs. 16 and 17.

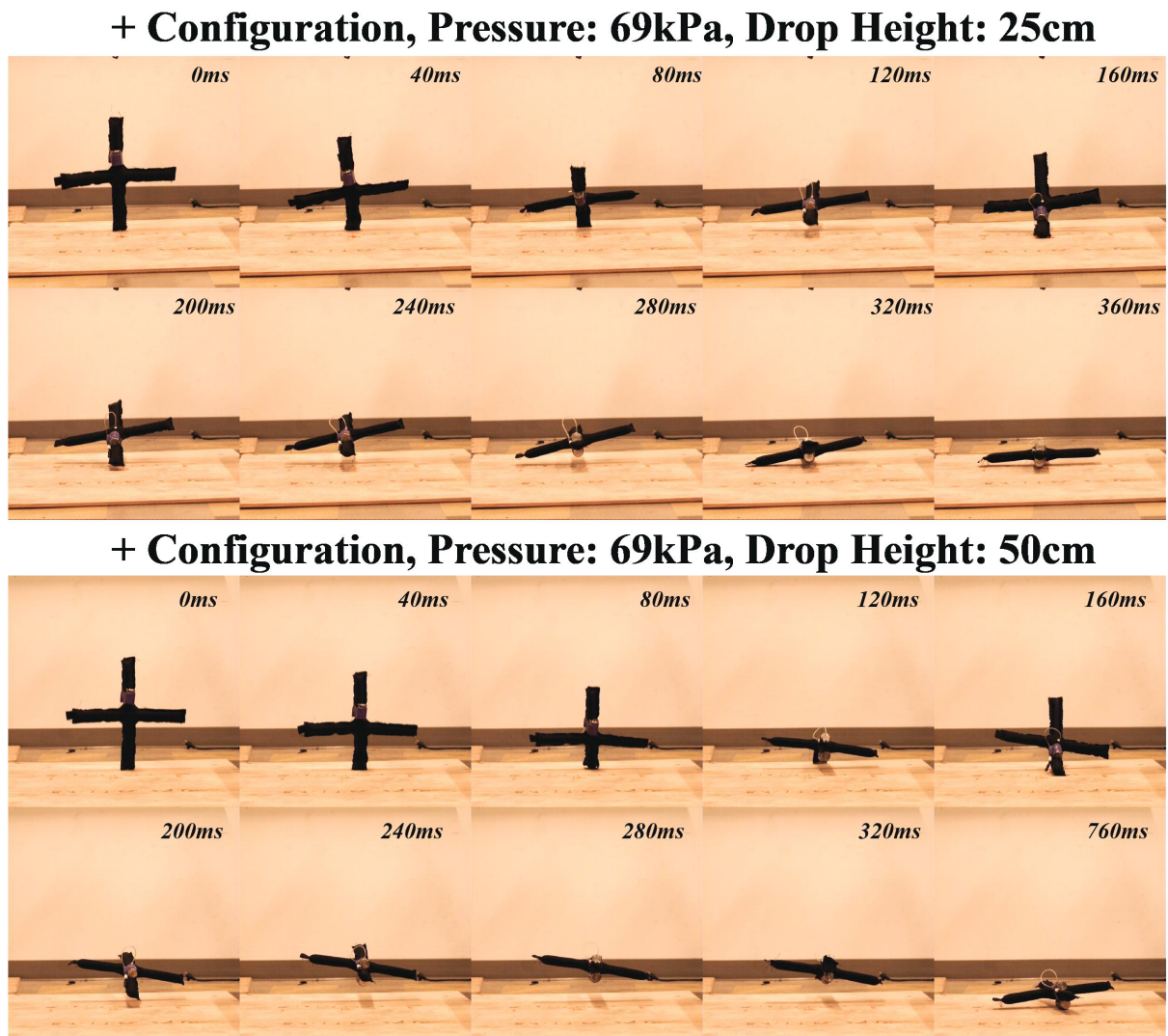
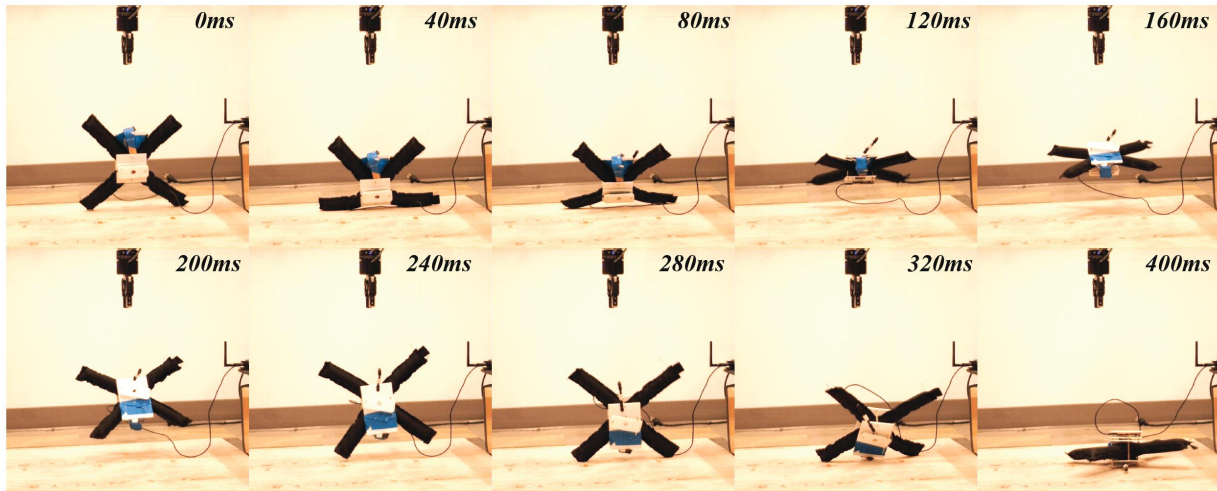


Fig. 12. Collision drop tests for SoBAR's soft-bodied frame in '+' configuration with internal pressures of 69kPa at 25 and 50cm drop heights.

X Configuration, Pressure: 69kPa, Drop Height: 25cm



X Configuration, Pressure: 69kPa, Drop Height: 50cm

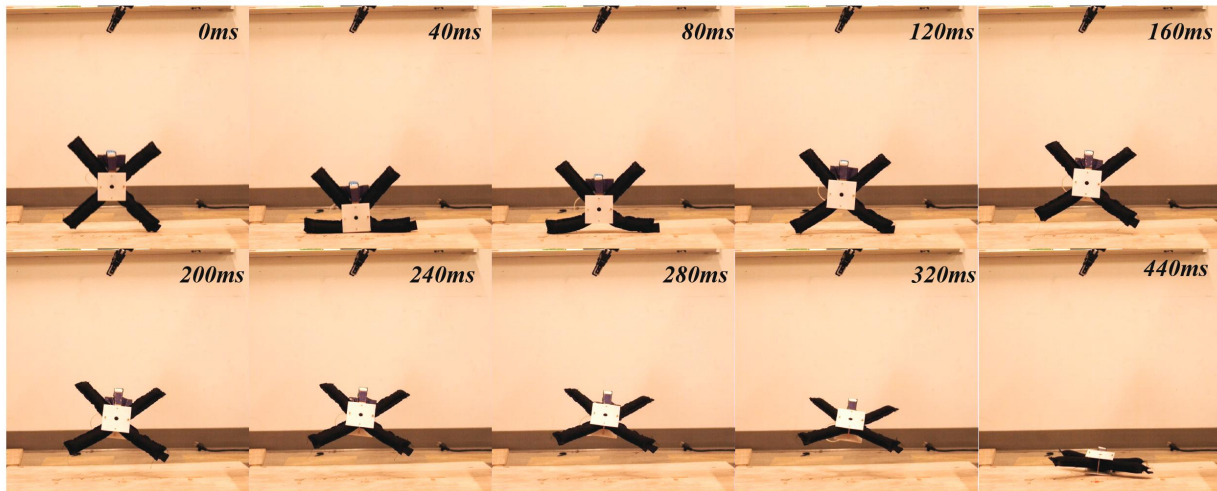


Fig. 13. Collision drop tests for SoBAR's soft-bodied frame in 'x' configuration with internal pressures of 69kPa at 25 and 50cm drop heights.

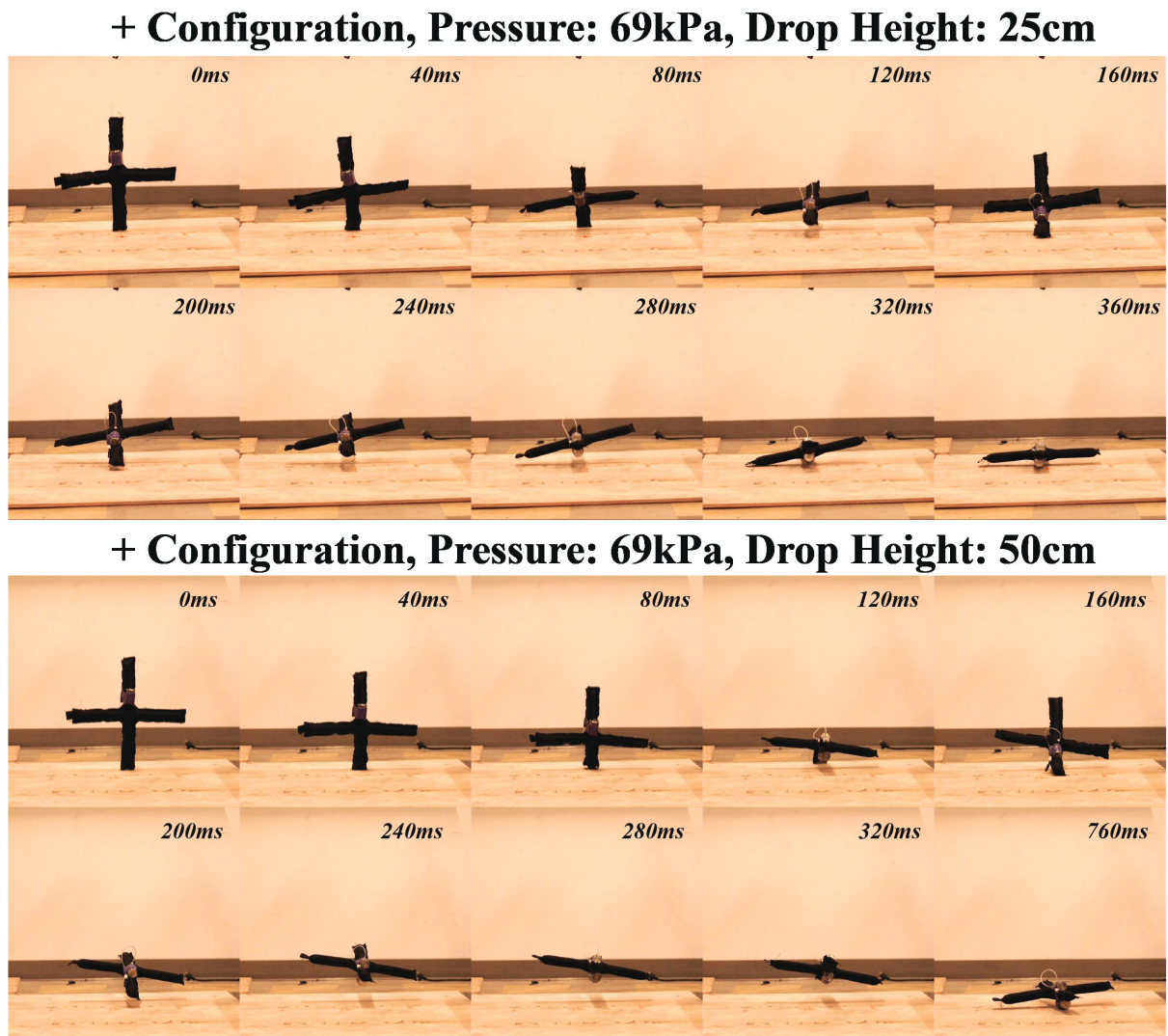
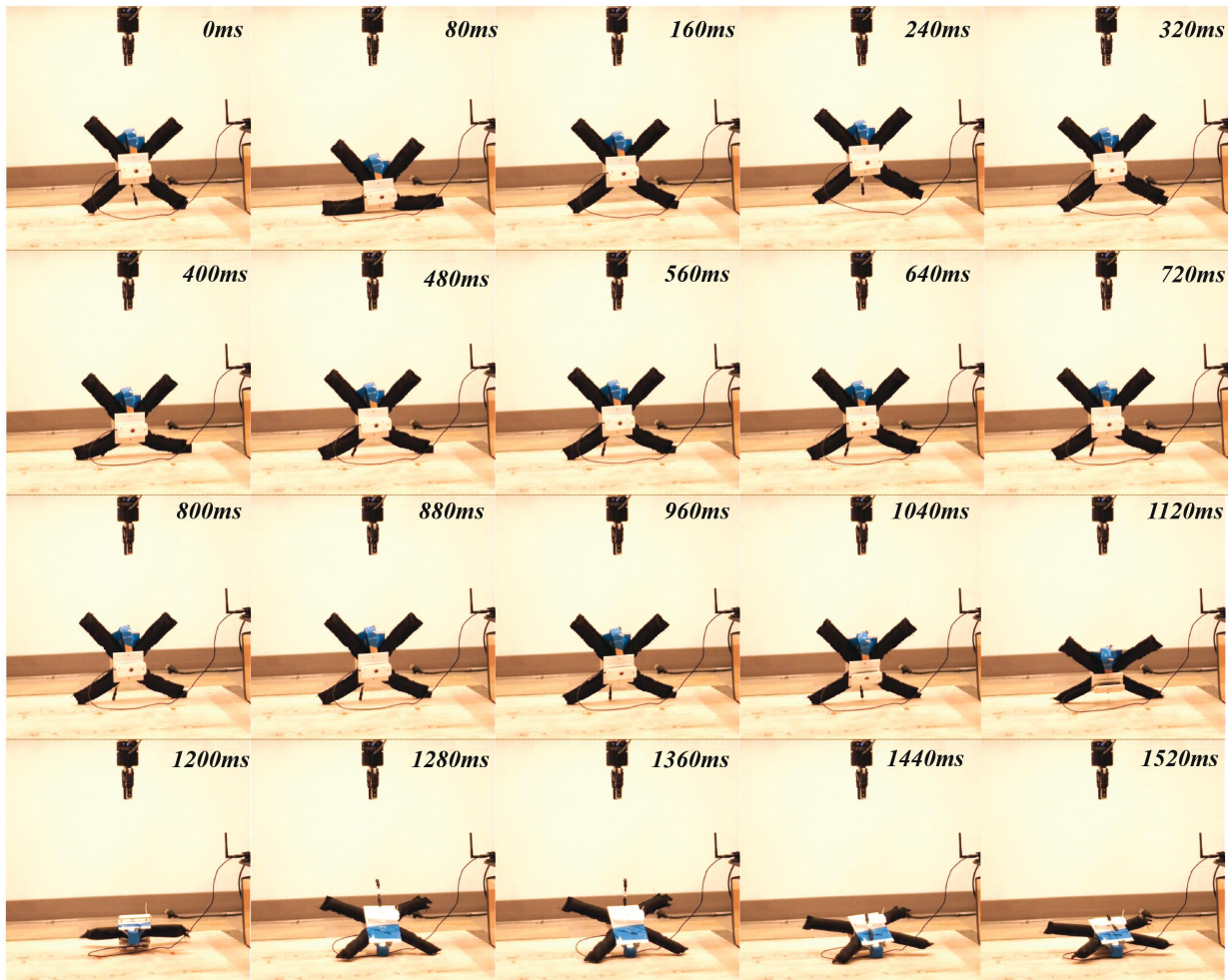


Fig. 14. Collision drop tests for SoBAR's soft-bodied frame in '+' configuration with internal pressures of 138kPa at 25 and 50cm drop heights.

X Configuration, Pressure: 138kPa, Drop Height: 25cm



X Configuration, Pressure: 138kPa, Drop Height: 50cm

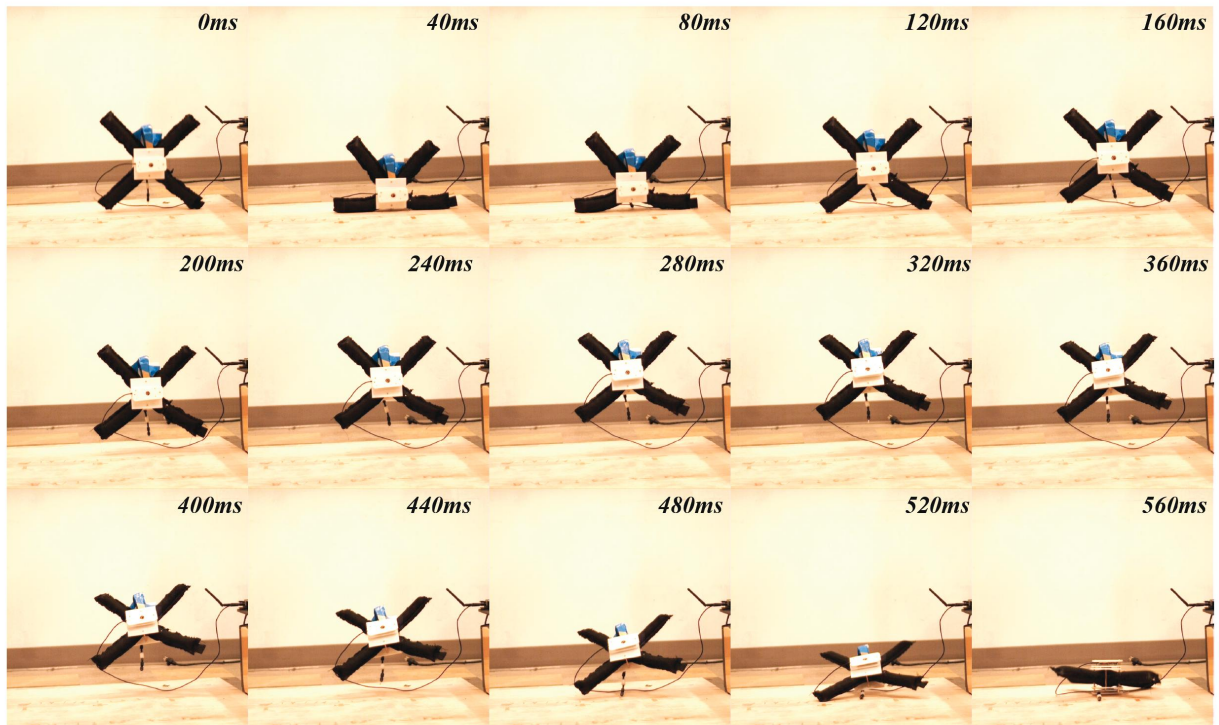
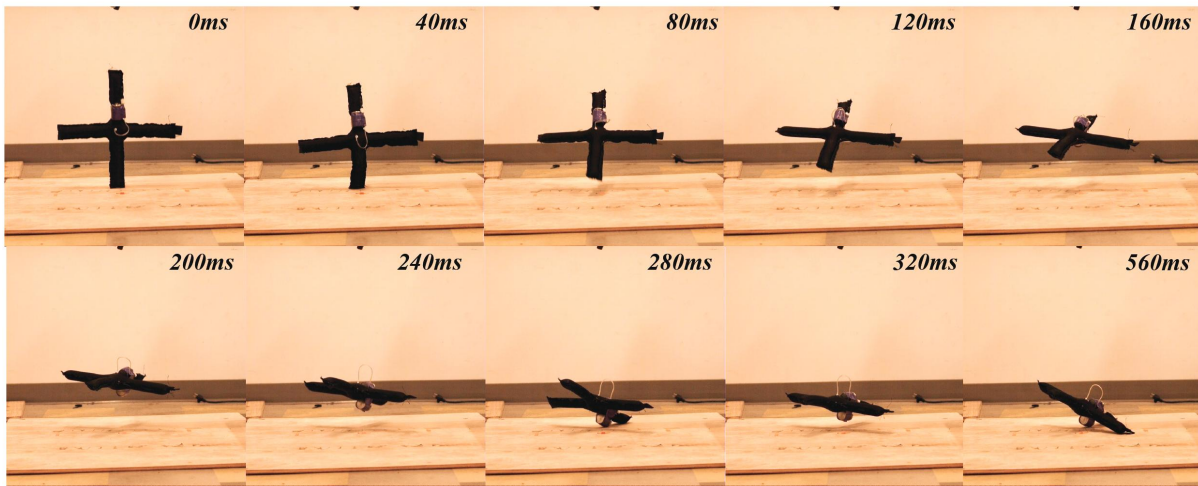


Fig. 15. Collision drop tests for SoBAR's soft-bodied frame in 'x' configuration with internal pressures of 138kPa at 25 and 50cm drop heights.

+ Configuration, Pressure: 207kPa, Drop Height: 25cm



+ Configuration, Pressure: 207kPa, Drop Height: 50cm

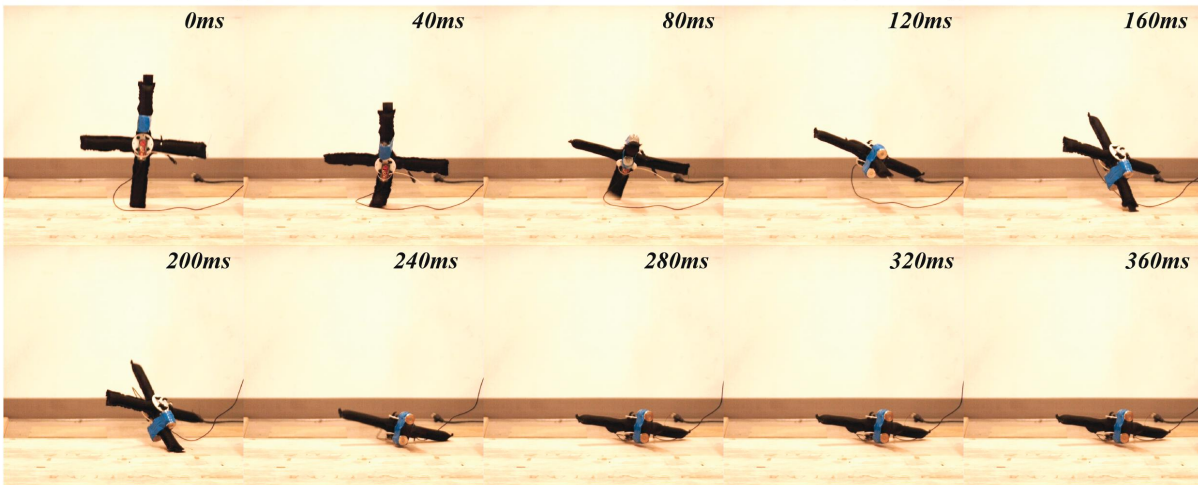
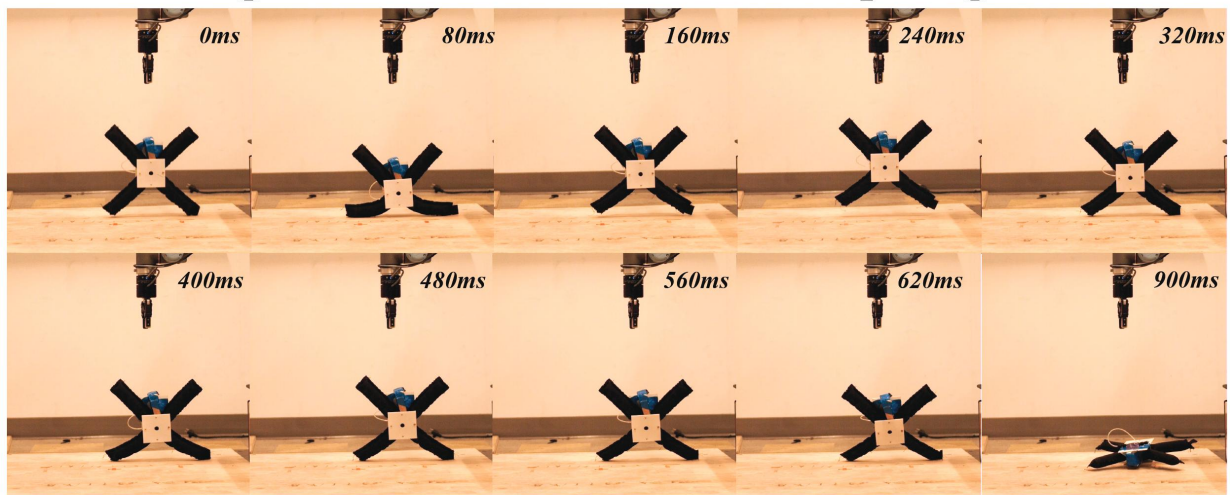


Fig. 16. Collision drop tests for SoBAR's soft-bodied frame in '+' configuration with internal pressures of 207kPa at 25 and 50cm drop heights.

X Configuration, Pressure: 207kPa, Drop Height: 25cm



X Configuration, Pressure: 207kPa, Drop Height: 50cm

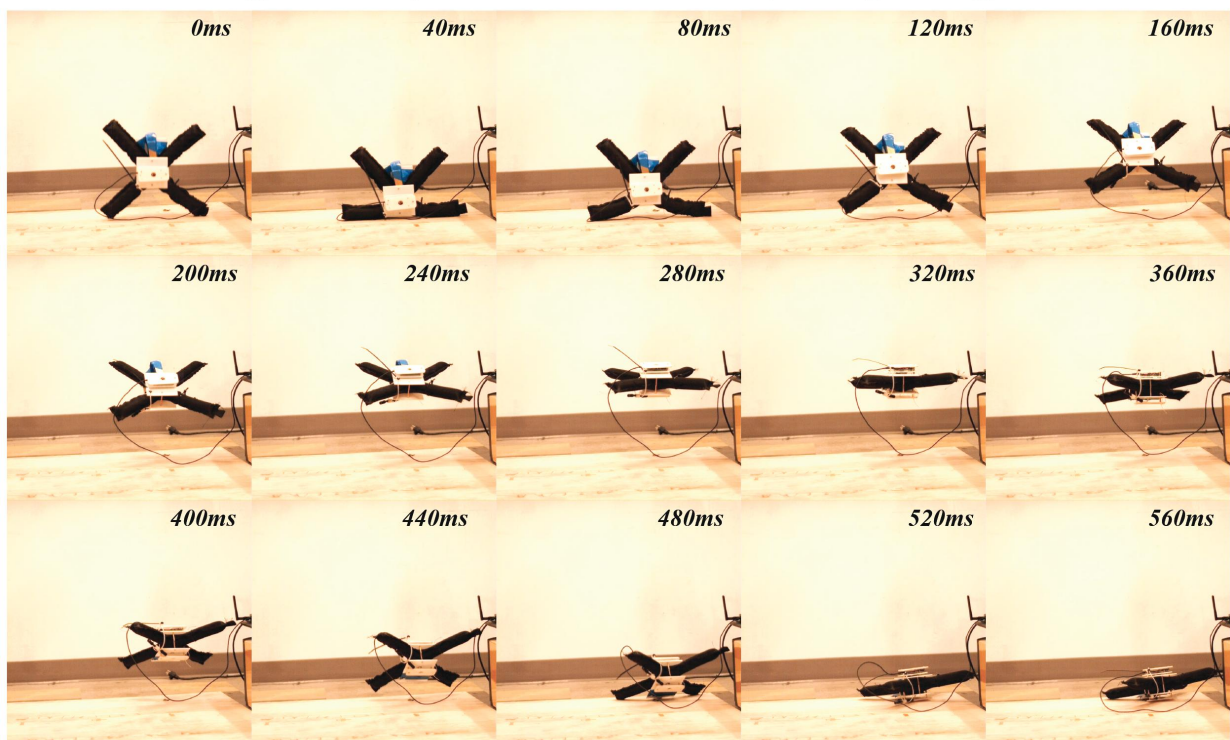


Fig. 17. Collision drop tests for SoBAR's soft-bodied frame in 'x' configuration with internal pressures of 207kPa at 25 and 50cm drop heights.